Thermally Stable Ni-rich Austenite Formed Utilizing Multistep Intercritical Heat Treatment in a Low-Carbon 10 Wt Pct Ni Martensitic Steel

DIVYA JAIN, DIETER ISHEIM, XIAN J. ZHANG, GAUTAM GHOSH, and DAVID N. SEIDMAN

Austenite reversion and its thermal stability attained during the transformation is key to enhanced toughness and blast resistance in transformation-induced-plasticity martensitic steels. We demonstrate that the thermal stability of Ni-stabilized austenite and kinetics of the transformation can be controlled by forming Ni-rich regions in proximity of pre-existing (retained) austenite. Atom probe tomography (APT) in conjunction with thermodynamic and kinetic modeling elucidates the role of Ni-rich regions in enhancing growth kinetics of thermally stable austenite, formed utilizing a multistep intercritical (*Quench-Lamellarization-Tempering* (QLT)-type) heat treatment for a low-carbon 10 wt pct Ni steel. Direct evidence of austenite formation is provided by dilatometry, and the volume fraction is quantified by synchrotron X-ray diffraction. The results indicate the growth of nm-thick austenite layers during the second intercritical tempering treatment (T-step) at 863 K (590 °C), with austenite retained from first intercritical treatment (L-step) at 923 K (650 °C) acting as a nucleation template. For the first time, the thermal stability of austenite is quantified with respect to its compositional evolution during the multistep intercritical treatment of these steels. Austenite compositions measured by APT are used in combination with the thermodynamic and kinetic approach formulated by Ghosh and Olson to assess thermal stability and predict the martensite-start temperature. This approach is particularly useful as empirical relations cannot be extrapolated for the highly Ni-enriched austenite investigated in the present study.

I. INTRODUCTION

HIGH-PERFORMANCE structural materials are needed for U. S. Naval applications, such as ship hulls and decks, which require an excellent combination of strength, low-temperature impact toughness, ductility, blast resistance, and weldability.[1–4] In recent years, several research efforts have been performed, to develop alternatives to the widely used Naval HSLA-100 steels with a superior yield strength and blast resistance to reduce the weight of structural components and pre-empt increasing terrorist threats.[3,5–11] Optimizing the overall mechanical properties for such applications entails several design challenges; most importantly, increasing the strength invariably leads to concomitant deterioration in toughness and ductility. The concept of transformation-induced-plasticity (TRIP) has been commonly utilized to combine high-strength in martensitic steels with good toughness[12–14] and to enhance ductility in automotive steels.[15–17] TRIP utilizes deformation-induced martensitic transformations to enhance plasticity of alloys.[18–20] The benefits of transformation toughening and enhanced ductility from such martensitic transformations rely on the volume fraction and relative stability of austenite, which can be tailored by optimizing the chemical compositions and heat treatments of steels.

Low-carbon steels (<0.1 wt pct C) are preferred for Naval structural applications for good weldability and low-processing costs.[21,22] Thus, unlike the advanced high-strength quench and partitioning steels, which rely on carbon partitioning for stabilizing austenite,[23,24] the steel investigated in the present study is a low-carbon (0.09 wt pct) 10 wt pct Ni-Cr-Mo-V steel, which utilizes Ni as the primary austenite stabilizer. Additionally, Ni

DIVYA JAIN and GAUTAM GHOSH are with Northwestern University, Department of Materials Science & Engineering, 2220 Campus Drive, Evanston, IL 60208. Contact e-mail: divyajain2016@u.northwestern.edu DIETER ISHEIM and DAVID N. SEIDMAN are with Northwestern University, Department of Materials Science & Engineering, and also with Northwestern University Center for Atom-Probe Tomography (NUCAPT), 2220 Campus Drive, Evanston, IL 60208. XIAN J. ZHANG is with the Carderock Division, Naval Surface Warfare Center, West Bethesda, MD 20817.

additions in steels are also believed to lower the ductile-to-brittle transition temperatures in steels due to its effect on cross-slip of dislocations[25] and/or on the cohesive energy of iron at low temperatures.[26] Recent dilatometry and microhardness characterization of a similar steel containing 9 wt pct Ni reported martensitic microstructures after solutionizing and quenching treatment (for a wide range of cooling rates).[27] A common processing route to form Ni-rich austenite in significant volume fractions from the as-quenched microstructure is to employ intercritical heat treatments in the ferrite (α) plus austenite (γ) two-phase field. Low-carbon (<0.1 wt pct) steels containing 5 to 9 wt pct Ni have been in use for several decades for cryogenic applications and are processed by similar single or multistep intercritical treatments.[28–36]

In the present study, we utilize a *Quench-Lamellarization-Tempering* (QLT) heat treatment, where 'L' and 'T' refer to the intercritical isothermal treatments in the upper and lower range of the α plus γ dual-phase field, employed after the solutionizing and quenching step (Q). Detailed evaluation of the mechanical properties of this steel after the optimal QLT-treatment revealed an excellent combination of yield strength, 130 ksi (896.3 MPa), ultimate tensile strength, 158 ksi (1089.4 MPa), an elongation to failure of 23 pct, a Charpy impact toughness of 153 J at 188.7 K (-84.4 °C), and a 18 pct higher ballistic limit, V_{50} than the widely used HSLA-100 steels for Naval structural applications.[8] Its superior ballistic resistance is attributed to its enhanced dynamic plasticity, due to the deformation-induced martensitic transformation of the dispersed austenitic phase.[8] In this article, we study the basic physical principles behind the multistep intercritical treatment; specifically, the thermal stability and formation kinetics of reverted austenite using dilatometry, synchrotron X-ray diffraction, ultraviolet (wavelength = 355 nm) laser-assisted 3-D atom probe tomography (APT), and computational modeling tools, ThermoCalc[37,38] and DICTRA.[38,39]

APT is a unique analytical technique that provides 3-D spatial information of atoms and concurrently their chemical identities with sub-nanometer spatial resolution.[40–42] Investigating the microstructure at the sub-nanometer scale is crucial as the very small diffusivity of substitutional austenite stabilizers (for example, Ni or Mn) in austenite at the intercritical temperatures leads to local chemical concentration gradients, which are directly related to austenite reversion and its stability.[35,43,44] The composition of intercritically formed austenite measured employing 3-D APT is used to predict the martensite-start (M_s) temperature. The M_s temperature is an important design parameter to estimate the thermodynamic stability of austenite, which is primarily dependent on the composition of austenite.[45–48] We utilize the Ghosh–Olson thermodynamic and kinetic approach,[49–51] which integrates computational thermodynamics and the Olson–Cohen barrierless martensite nucleation model[52] to predict the M_s temperature. It is also demonstrated that commonly used empirical relations are unable to predict the M_s temperature of the Ni-rich austenite phase formed after the QLT heat treatment. 3-D APT results in conjunction with DICTRA simulations are used to study the kinetics of austenite formation during the T-step.

II. EXPERIMENTAL METHODS

The overall chemical composition of the steel, as measured by optical emission spectroscopy (for metallic elements) and combustion infrared detection analyser (for carbon), is given in Table I. The steel was processed by vacuum induction melting (VIM) and cast into an ingot, which was heated to 1533 K (1260 °C), and then held for 7 hours in a gas-fired furnace with a flow of protective nitrogen gas. Then it was hot-rolled to 20.3 cm × 2.5 cm (8″ × 1″) plates with a finishing temperature of 1116 K (843 °C). The final QLT heat treatment employed consists of an austenitizing treatment at 1073 K (800 °C) for ~1 hour and water quenching to room temperature (Q), followed by the first intercritical heat treatment (L) at 923 K (650 °C) for 20 to 30 minutes and a second intercritical heat treatment (T) at 863 K (590 °C) for 1 hour. Each intercritical heating step is terminated by water quenching the specimen to room temperature. To follow the evolution of the microstructure at different stages of the QLT-treatment, we also examined the samples in the as-quenched (Q), quenched-and-L-step (QL), and quenched-and-T-step (QT) conditions.

Samples for metallography were prepared by standard mounting, grinding, and polishing methods with a final polish using 0.06-μm diameter colloidal silica, followed by etching with a 2 pct Nital solution. The dilatometric tests were performed using a Gleeble 3500 thermal system employing 9.5-mm diameter cylindrical specimens. High-intensity synchrotron X-ray diffraction (XRD) scans were performed on polished samples at the 5-IDB beam line at the Advanced Photon Source (Argonne National Laboratory, Argonne, IL, USA). Scans were performed from 2θ ranging from 9.995 to 33.500 deg; employing a step size of 0.015 deg, a count time of 3 s per step, and a wavelength of 0.71 Å. At each step, the sample was rocked through 0.75 deg in θ to reduce preferential orientation effects. A NIST standard sample containing 5.8 vol pct austenite was also analyzed under identical conditions for calibration purposes. The data analysis involving peak positions, integrated intensities, and background removal was performed utilizing MDI JADE 2010 software (Materials Data Inc.). The volume fractions of austenite were calculated employing the direct comparison method,[53] which involves comparing the integrated intensities of the $(111)_\gamma$, $(110)_\alpha$, $(200)_\gamma$, $(200)_\alpha$, and $(220)_\gamma$ reflections, and the error is determined based on counting statistics.[54]

Figure 1 shows SEM micrographs of QL, QT, and QLT-treated 10 wt pct Ni samples. In the QL and QLT-treated samples, the brighter phase protruding from the surface is a mixture of reverted austenite (formed during the intercritical treatment) and fresh-martensite, which resulted from the transformation of some of the reverted austenite during

Table I. Overall Chemical Composition of 10 Wt Pct Ni Steel

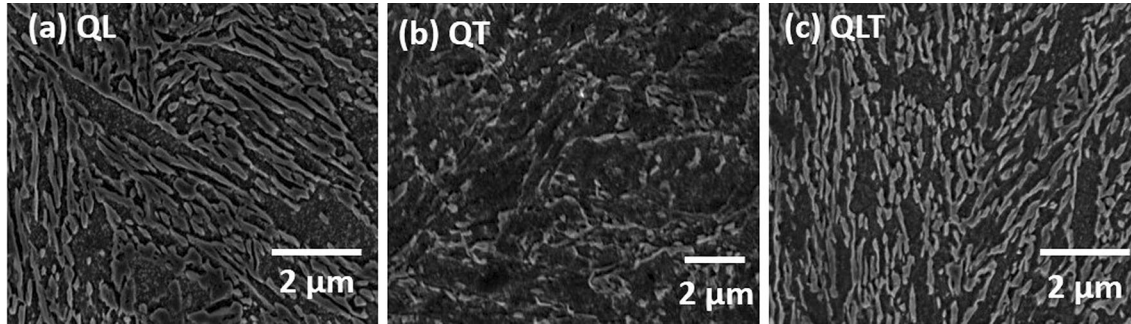| Elements	Fe	Ni	Mn	C	Si	Cr	Mo	Cu	V
Wt Pct	87.11	9.85	0.60	0.09	0.21	0.60	1.23	0.15	0.08
At. Pct	87.43	9.41	0.61	0.42	0.42	0.65	0.72	0.13	0.09

Fig. 1—SEM micrographs of (a) QL; (b) QT; and (c) QLT-treated 10 wt pct Ni steel etched with a 2 pct nital solution.

quenching.[8] During intercritical heating, a portion of the parent as-quenched martensite does not transform to austenite and is referred to as tempered martensite. The intercritically formed austenite (or fresh-martensite) phase protrudes from the surface as the tempered martensitic matrix is preferentially removed during etching.[43] We did not observe such dispersions of austenite (or fresh-martensite) in the QT-treated sample, Figure 1(b), as the microstructure consists predominantly of tempered martensite. Nanotips for 3-D APT investigations were prepared by a standard dual-beam focused-ion beam (FIB) microscopy lift-out preparation technique,[55] targeting the austenite (fresh-martensite) phase. Details of this method are provided in a prior article on 4.5 and 10 wt pct Ni steels.[43] 3-D APT experiments were performed with a Cameca local-electrode atom probe (LEAP) 4000X-Si tomograph, using ultraviolet (wavelength = 355 nm) picosecond laser pulsing with an energy of 30 pJ per pulse, a pulse repetition rate of 500 kHz, and an average evaporation rate (number of ions per pulse) of 2 pct. The samples were analyzed at a specimen base temperature of 60 K (-213 °C) in ultrahigh vacuum ($<10^{-8}$ Pa), and the data obtained were analyzed using the program IVAS 3.6 (Cameca, Madison, WI).

III. MARTENSITE-START (M_S) TEMPERATURE CALCULATIONS AND DICTRA SIMULATIONS

M_s temperature calculations corresponding to the austenite compositions obtained in the QL- and QLT-treated samples were performed using the Ghosh–Olson thermodynamic and kinetic approach,[49–51] based on the Olson–Cohen model,[52] in which the critical driving force for martensite nucleation, $\Delta G_{ch-crit}$, is expressed as

$$\Delta G_{ch-crit} = -[K + w_\mu + w_{th}], \quad [1]$$

where K is evaluated as 1010 J/mol and includes the strain and interfacial energies associated with

semicoherent nucleation of martensite, and w_μ and w_{th} are the athermal and thermal interfacial frictional work, respectively, required for the motion of dislocations.[49] The interfacial work terms are modeled based on the theory of solid-solution strengthening[56,57] and are given by Eqs. [2] and [3] given below:

$$w_\mu = \sqrt{\sum_i (k_\mu^i X_i^{0.5})^2} + \sqrt{\sum_j (k_\mu^j X_j^{0.5})^2}, \quad [2]$$

where X is the concentration (mole-fraction) of the solute elements, i = C, Cr, Mn, Mo, Si, and V, and j = Cu, Ni,[51] and the coefficients, k_μ for these elements are listed in Table II.

$$w_{th}(T) = w_o \left[1 - \left(T/T_\mu \right)^{1/q} \right]^{1/p} \quad [3]$$

where p = 0.5, q = 1.5, and $T_\mu \approx 500$ (in Kelvin)[50] and,

$$w_o = w_o^{Fe} + \sqrt{\sum_i (k_o^i X_i^{0.5})^2} + \sqrt{\sum_j (k_o^j X_j^{0.5})^2}, \quad [3a]$$

where i = C, Cr, Mn, Mo, Si, and V and j = Cu, Ni,[51] and w_o^{Fe} is the value of w_o for pure Fe and is evaluated as 836 J/mol,[50] and the coefficients, k_o for these elements are listed in Table II.

For a given austenite composition, X and temperature, T, the volume free energy change associated with compositionally invariant martensitic transformation, $\Delta G_{ch}(T, X)$ is calculated using ThermoCalc; version S employing the kMART thermodynamic database.[51,58] M_s temperature is then calculated to be the temperature at which,

$$\Delta G_{ch}(T, X) = \Delta G_{ch-crit} \quad [4]$$

Kinetic simulations using DICTRA were performed for Fe-Ni system using the mobFe1 mobility database

Element	k_μ (J/mol)	k_o (J/mol)
C	3807	21,216
Mn	1980	4107
Si	1879	3867
Cr	1868	3923
V	1618	3330
Mo	1418	2918
Cu	752	1548
Ni	172	345

and the *TCFe6 thermodynamic database*. A linear cell geometry is chosen with fixed dimensions, which is commonly used to study austenite/ferrite diffusional transformations in steels.[39,59,60] The DICTRA cell consists of different regions, which represent different phases and are separated by mobile planar boundaries.[39,60] Simulations are performed assuming local equilibrium conditions at these heterophase boundaries, which implies infinite interface mobility and results in the transformation kinetics being controlled by the diffusion of Ni.

IV. RESULTS

A. *Dilatometry*

Figure 2 shows the dilatometric response of the QLT-treated 10 wt pct Ni steel during intercritical treatments. The observed contraction during the isothermal steps at 923 K and 863 K (650 °C and 590 °C) indicates the formation of austenite during these L- and T-steps, respectively. During quenching, following the isothermal step at 923 K (650 °C), we observe that the sample begins to expand at ~461 K (188 °C), indicating the onset of a martensitic transformation. This temperature is thus the M_s temperature for the austenite formed during the L-step. The sample does not expand during quenching following the T-step, indicating that the austenite after tempering at 863 K (590 °C) has a greater thermal stability than the austenite formed during the L-step.

B. *Synchrotron X-ray Diffraction (XRD)*

High-intensity synchrotron X-ray diffraction (XRD) scans of the 10 wt pct Ni steel samples after different stages of the QLT-treatment are displayed in Figure 3. The volume fraction of austenite measured in the NIST standard is 5.4 ± 0.1 pct, while the calibrated standard value is 5.8 pct. The volume fractions of austenite after calibration for the as-quenched, QT, QL, and QLT-treated samples are 1.5, 2.9, 8.1, and 18.5 vol pct, respectively, Table III. We also obtained a volume fraction of ~18 pct for the QLT-treated sample that was subsequently quenched to 188.7 K (−84.4 °C), prior to the XRD investigation. This indicates that austenite after the T-step is thermally stable and its M_s temperature is less than 188.7 K (−84.4 °C).
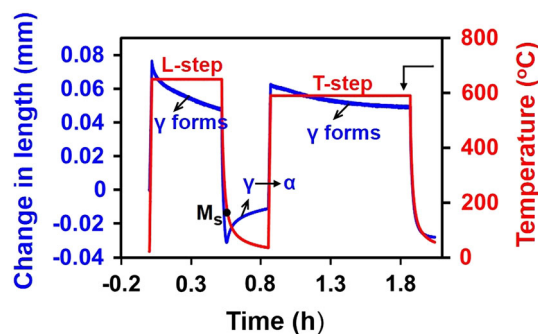

Fig. 2—Dilatometric responses of the 10 wt pct Ni steel (in blue) exhibiting austenite formation during intercritical isothermal steps at 923 K and 863 K (650 °C and 590 °C). Some of the austenite transforms to martensite during quenching, after isothermal aging at 923 K (650 °C). This transformation commences at 461 K (188 °C), the martensite-start (M_s) temperature (Color figure online).
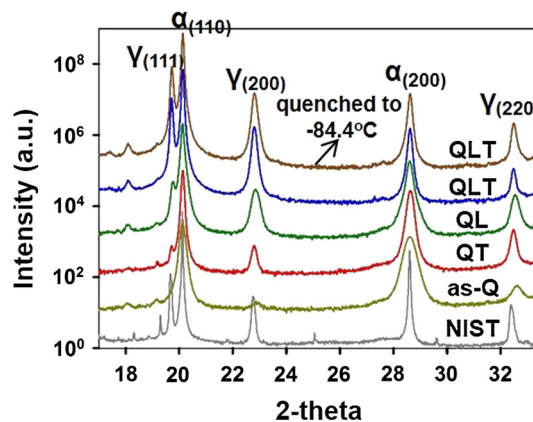

Fig. 3—Synchrotron X-ray diffraction scans of the 10 wt pct Ni steel after different stages of the QLT-treatment, including the QLT-treated sample that was subsequently quenched to 188.7 K (−84.4 °C), prior to the X-ray diffraction analysis. The NIST standard sample is also analyzed for calibration purposes.

Table III. Volume Percent of Austenite in 10 Wt Pct Ni Steel Samples After Different Stages of the QLT-Treatment, as Obtained by Synchrotron X-ray Diffraction (XRD) Experiments Performed at the Advanced Photon Source at Argonne National Laboratory

	As-Quenched	QT	QL	QLT	QLT (Quenched to 188.7 K (−84.4 °C), Prior to XRD)
Vol Pct	1.5 ± 0.5	2.9 ± 0.2	8.1 ± 0.3	18.5 ± 0.2	18.0 ± 0.2

C. *3-D Atom Probe Tomography (APT)*

1. *APT analyses of the QL-treated samples*

Figures 4(a) and (b) display the 3-D APT reconstructions of the QL-treated steel, in which Fe atoms are displayed in blue and Ni atoms are in green. We also observe mixed metal carbides of MC and M_2C-type in

QL-nanotip 1   QL-nanotip 2

α-Fe

α-Fe

Metal Carbide precipitates

Ni-rich

Ni-rich

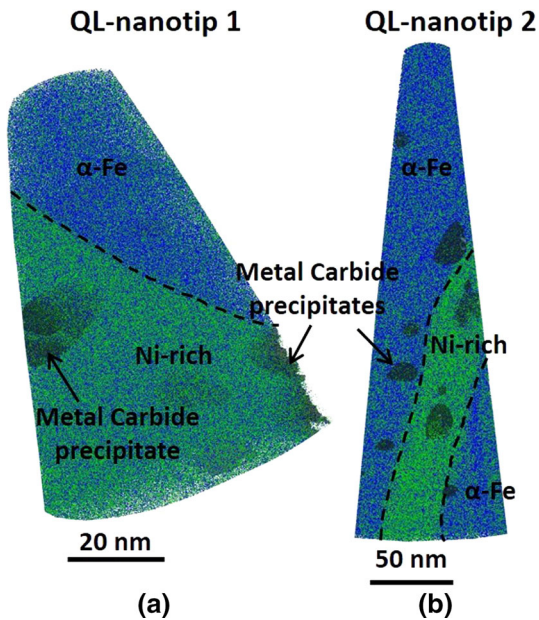Metal Carbide precipitate

α-Fe

20 nm

50 nm

(a)   (b)

Fig. 4—3-D APT reconstructions of the QL-treated 10 wt pct Ni steel: (*a*) QL-1 sample, Fe atoms (10 pct) are displayed as blue dots, Ni atoms (100 pct) are displayed in green; (*b*) QL-2 sample, Fe atoms (3 pct) are displayed as blue dots, Ni atoms (30 pct) are displayed in green. The heterophase interface (indicated by a dashed curve) between the tempered martensite matrix, α-Fe, and the Ni-rich region is delineated by 9 and 11 at. pct Ni isoconcentration surfaces in (a) and (b), respectively. Metal carbides are delineated by a 10 at. pct (C plus Cr plus Mo plus V) isoconcentration surfaces (black) in both reconstructions (Color figure online).

both APT reconstructions; these carbides are displayed in black, and are rich in Mo, Cr, and V. During the austenite formation at 923 K (650 °C), Ni partitions to austenite and it is depleted in the tempered martensite matrix, α-Fe,

which is richer in Fe and thus appears in blue in Figure 4. We note that some of the austenite formed during the L-step transforms to martensite during quenching, as is revealed by dilatometry (Figure 2). We refer to this martensite as fresh-martensite, whose composition is assumed to be the composition of the reverted austenite formed at 923 K (650 °C). This assumption is reasonable as the martensitic transformation is compositionally invariant and commences at a relatively low temperature in the QL-treated sample, 461 K (188 °C), below which the diffusion of solute elements (especially substitutional) in austenite or martensite during quenching is negligible. Kim *et al.*[36] also obtained similar composition of fresh-martensite as reverted austenite in a 5.5 wt pct Ni steel [intercritically annealed at 943 K (670 °C)] using energy-dispersive X-ray spectroscopy (EDS) in a scanning transmission electron microscope (STEM). Thus, the composition of the Ni-rich region in the APT reconstructions in Figure 4 represents the composition of austenite formed at 923 K (650 °C) and is obtained using a proximity histogram (or proxigram for short),[61] which measures the concentrations of each element as a function of distance from a specified isoconcentration surface. Since we want to determine the concentration profiles of elements only in the α-Fe matrix and the Ni-rich region, the metal carbides observed in the 3-D reconstructions were excluded from the dataset, using the IVAS code before obtaining the proximity histograms. The resulting proximity histogram concentration profiles for the QL-1 and QL-2 samples, obtained from 9 and 11 at. pct Ni isoconcentration surfaces, Figure 4, are displayed in Figures 5(a) and (b), respectively, and they reveal the enrichment of Ni, Mn, C, Cr, and Cu in austenite (toward the right-hand side of the vertical fiducial marker). While Ni, Mn, C, and Cu are
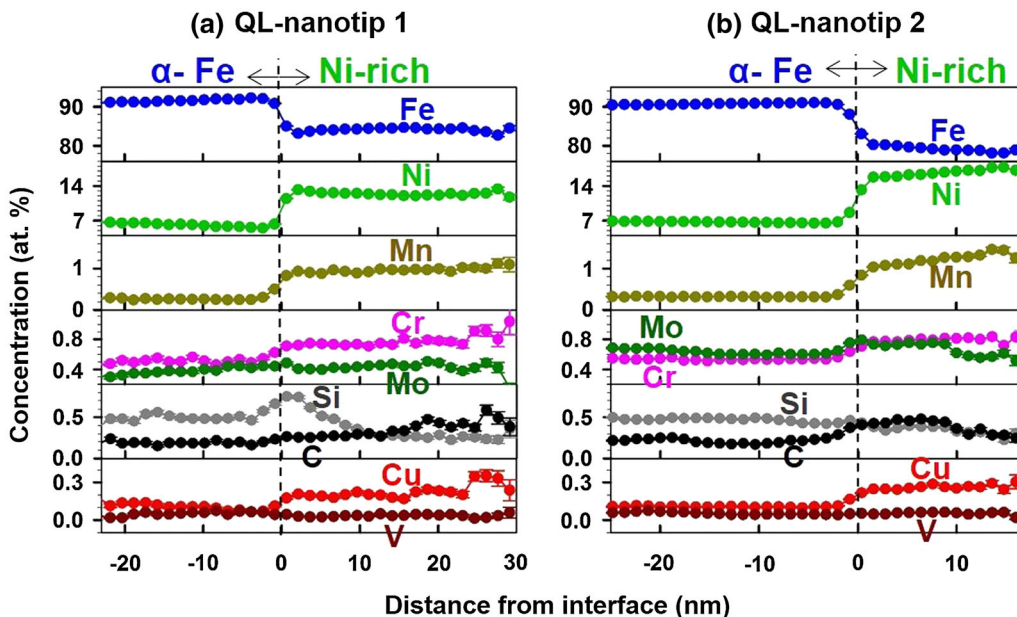

Fig. 5—Proximity histogram concentration profiles obtained from 9 and 11 at. pct Ni isoconcentration surfaces in (*a*) QL-1 and (*b*) QL-2 10 wt pct Ni steel samples, respectively, displaying the concentration profiles of Fe, Ni, Mn, Cr, Mo, Si, C, Cu, and V across the α-Fe matrix and Ni-rich region. Metal carbides were excluded from the datasets before obtaining the proximity histograms.

Table IV. Chemical Compositions (Atomic Percent) of Ni-rich Region [Austenite Formed During L-Step at 923 K (650 °C)] and the Tempered Martensite Matrix, α-Fe in the QL-Treated 10 Wt Pct Ni Steel, as Measured by APT. Martensite-Start (M_s) Temperatures, as Calculated Using the Ghosh–Olson Thermodynamic and Kinetic Approach Are also Shown

QL	Fe	Ni	Mn	C	Si	Cr	Mo	Cu	V	M_s K (°C)
Nanotip 1 (APT)										
Austenite at L-Step	84.06 ± 0.26	12.50 ± 0.23	0.96 ± 0.07	0.36 ± 0.04	0.35 ± 0.04	0.77 ± 0.06	0.43 ± 0.05	0.23 ± 0.04	0.04 ± 0.01	459.6 (186.5)
Tempered Martensite, α-Fe	90.98 ± 0.22	6.73 ± 0.19	0.26 ± 0.04	0.21 ± 0.04	0.46 ± 0.05	0.50 ± 0.05	0.34 ± 0.04	0.14 ± 0.03	0.03 ± 0.01	
Nanotip 2 (APT)										
Austenite at L-Step	79.22 ± 0.16	16.68 ± 0.15	1.23 ± 0.04	0.39 ± 0.02	0.34 ± 0.02	0.79 ± 0.03	0.67 ± 0.03	0.26 ± 0.02	0.06 ± 0.01	345 (71.9)
Tempered Martensite, α-Fe	90.54 ± 0.05	6.83 ± 0.05	0.32 ± 0.01	0.23 ± 0.01	0.48 ± 0.01	0.53 ± 0.01	0.66 ± 0.01	0.11 ± 0.01	0.06 ± 0.004	
ThermoCalc 923 K (650 °C)										
Austenite	85.53	11.80	0.80	0.18	0.48	0.68	0.31	0.17	0.006	
α-Fe	95.47	3.23	0.09	0.003	0.28	0.51	0.27	0.03	0.016	

Compositions of austenite and α-Fe, obtained from equilibrium thermodynamic calculations at 923 K (650 °C) using ThermoCalc are also listed.

well-known austenite stabilizers,[62] the partitioning of Cr in austenite is noteworthy, which has been observed in an APT investigation of 4.5 and 10 wt pct Ni steels, and was attributed to metastable equilibrium between austenite and martensite in the absence of the ferrite phase.[43]

The average compositions obtained for the α-Fe matrix and austenite from these proximity histograms are listed in Table IV and the error reported is ±σ, where σ is obtained from counting statistics,[63] and is expressed as

$$\sigma = \sqrt{\frac{c_i(1 - c_i)}{N}} \qquad [5]$$

where c_i is the measured concentration of element i in a sampled volume containing N total number of atoms. The compositions of α-Fe matrix and austenite from equilibrium thermodynamic calculations at 923 K (650 °C) using ThermoCalc are also presented in Table IV. Austenite in the QL-treated samples is primarily enriched in Ni (12.5 to 16.7 at. pct) and contains much smaller concentrations of the other solute elements, ~0.4C-1.1Mn-0.8Cr-0.3Si-0.6Mo-0.2Cu at. pct, Table IV. The enrichment of C (strong austenite stabilizer) in austenite is small (0.4 at. pct) due to its overall small concentration in steel (0.4 at. pct), coupled with the simultaneous precipitation of metal carbides during the intercritical treatment. In this article, we discuss in detail below, primarily, the partitioning behavior of Ni across the austenite and α-Fe matrix heterophase interface during the QLT-treatment.

2. APT analyses of the QLT-treated samples

3-D APT reconstructions of the QLT-1 and QLT-2 samples are displayed in Figures 6(a) and (b),

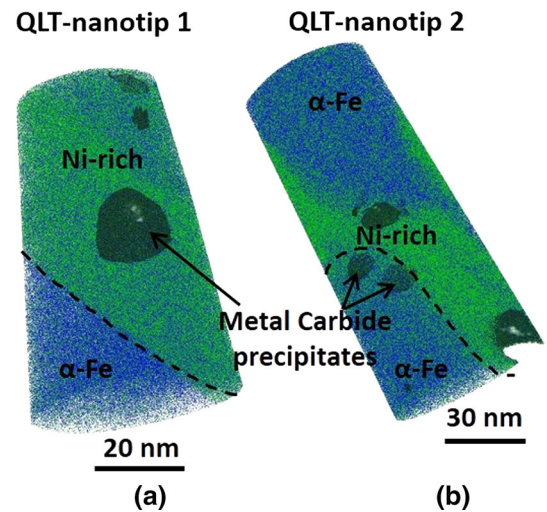**QLT-nanotip 1**   **QLT-nanotip 2**

Fig. 6—3-D APT reconstructions of the QLT-treated 10 wt pct Ni steel: (a) QLT-1 sample, Fe atoms (10 pct) are displayed as blue dots, Ni atoms (80 pct) are displayed in green; (b) QLT-2 sample, Fe atoms (5 pct) are displayed as blue dots, Ni atoms (50 pct) are displayed in green. The heterophase interface (indicated by a dashed curve) between the tempered martensite matrix, α-Fe, and the Ni-rich region is delineated by 11 at. pct Ni isoconcentration surface in both (a) and (b). Metal carbides are delineated by a 10 at. pct (C plus Cr plus Mo plus V) isoconcentration surfaces (black) in both reconstructions (Color figure online).
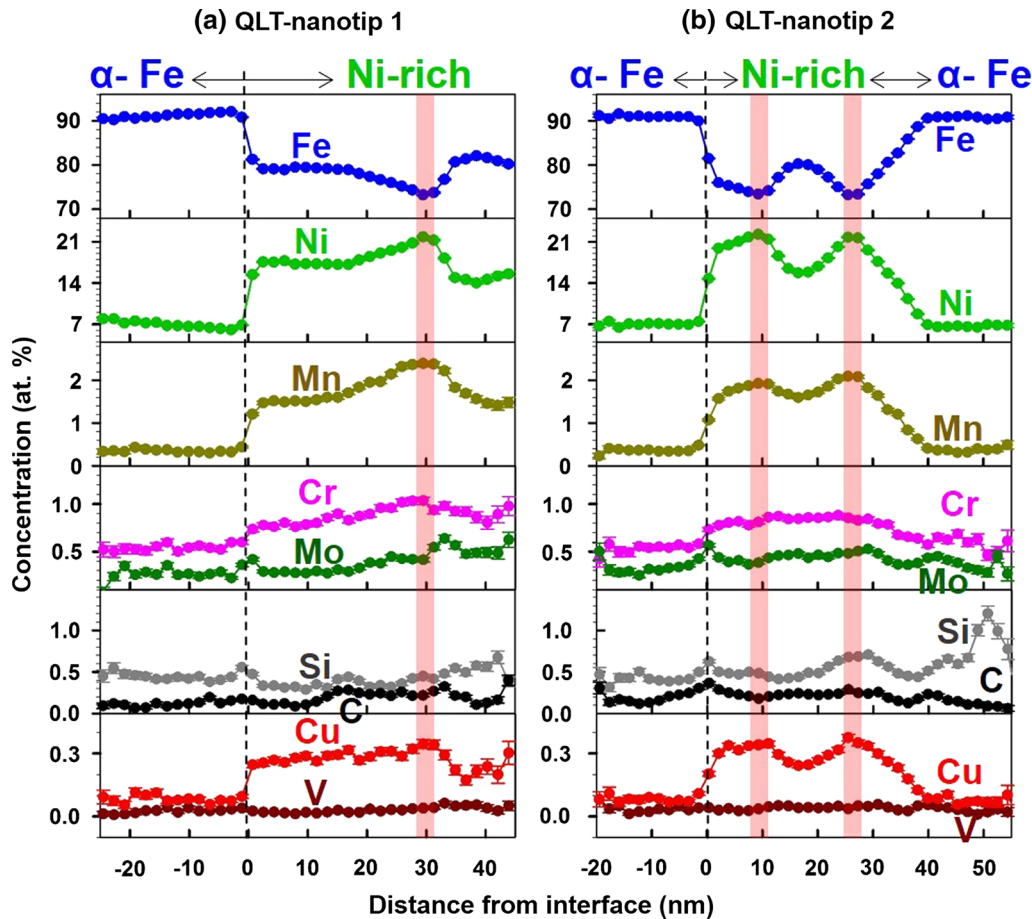
Fig. 7—Proximity histogram concentration profiles obtained from 11 at. pct Ni isoconcentration surfaces in (*a*) QLT-1 and (*b*) QLT-2 10 wt pct Ni steel samples, displaying the concentration profiles of Fe, Ni, Mn, Cr, Mo, Si, C, Cu, and V across the α-Fe matrix and Ni-rich region. Metal carbides were excluded from the dataset before obtaining the proximity histograms. Shaded regions on the Ni-rich side in (a) and (b) represent the composition of austenite formed during the T-step tempering at 863 K (590 °C).

respectively. The heterophase interface between α-Fe and the Ni-rich region (indicated by a dashed curve) in these APT reconstructions is delineated by 11 at. pct Ni isoconcentration surfaces. As in the QL-treated samples, we observe mixed metal carbides enriched in Mo, Cr, and V of MC- and M_2C-types in both QLT-treated samples. Proximity histogram concentration profiles obtained from the 11 at. pct Ni isoconcentration surfaces in QLT-1 and QLT-2 samples (after excluding the metal carbides from the dataset) are displayed in Figures 7(a) and (b), respectively.

In Figure 7(a), we observe significant inhomogeneities in the Ni concentrations within the Ni-rich region (right-hand side of the vertical fiducial marker in the proximity histogram). Ni-rich region in this proximity histogram is, therefore, divided into three regions having different Ni concentrations; the region with the highest Ni concentration is shaded in the proximity histogram and has an average Ni concentration of 21.7 at. pct, and the two regions to the left-and right-hand sides of this shaded region have average Ni concentrations of 17.7 and 14.6 at. pct, respectively. Table V lists the overall compositions of

these Ni-rich regions along with the composition of α-Fe and the error reported is ±σ, where σ is determined from Eq. [5]. The inhomogeneous distri-bution of Ni is also observed in the Ni-rich region in the proximity histogram corresponding to the QLT-2 sample, Figure 7(b). The shaded regions in the prox-imity histogram have an average Ni concentration of 21.9 at. pct, while the average Ni concentration in the plateau region between these shaded regions is 15.9 at. pct. Table V lists the overall compositions of these regions along with the composition of α-Fe. Similar trends as described for Ni is also observed for the Mn and Cu concentration profiles in both the proximity histograms in Figure 7. Compositions of austenite and α-Fe from equilibrium thermodynamic calculations at 863 K (590 °C) using ThermoCalc are also presented in Table V. The inhomogeneous distributions of these elements are a result of the austenite forming with different compositions during intercritical treat-ments at 923 K and 863 K (590 °C and 650 °C), coupled with sluggish diffusion of these elements in austenite, which is discussed in more detail in Section V–A–2.

Table V. Chemical Compositions (Atomic Percent) of Ni-rich Regions [Austenite Formed During T-Step at 863 K (590 °C) and Retained Austenite from L-Step at 923 K (650 °C)] and the Tempered Martensite Matrix, α-Fe in the QLT-Treated 10 Wt Pct Ni Steel Samples, as Measured by APT. Martensite-Start (M_s) Temperatures, as Calculated Using the Ghosh–Olson Thermodynamic and Kinetic Approach Are also Shown

QLT	Fe	Ni	Mn	C	Si	Cr	Mo	Cu	V	M_s [K (°C)]
Nanotip 1 (APT)										
Austenite at T-Step	73.37 ± 0.31	21.73 ± 0.29	2.40 ± 0.11	0.20 ± 0.03	0.45 ± 0.05	0.99 ± 0.07	0.43 ± 0.05	0.33 ± 0.04	0.04 ± 0.01	125.7 (−147.4)
Austenite from L-step [Left of Shaded Region, Fig. 7(a)]	79.15 ± 0.24	17.34 ± 0.22	1.55 ± 0.07	0.16 ± 0.02	0.35 ± 0.03	0.80 ± 0.05	0.29 ± 0.03	0.28 ± 0.03	0.02 ± 0.01	332.8 (59.7)
Austenite from L-step [right of shaded region, Fig. 7(a)]	81.40 ± 0.52	14.62 ± 0.48	1.58 ± 0.17	0.15 ± 0.05	0.57 ± 0.10	0.88 ± 0.13	0.48 ± 0.09	0.23 ± 0.06	0.05 ± 0.03	390.8 (117.7)
Tempered Martensite, α-Fe	90.65 ± 0.41	7.52 ± 0.37	0.37 ± 0.08	0.08 ± 0.03	0.46 ± 0.09	0.52 ± 0.10	0.25 ± 0.07	0.09 ± 0.04	0.02 ± 0.01	
Nanotip 2 (APT)										
Austenite at T-Step	73.43 ± 0.16	21.89 ± 0.15	2.00 ± 0.05	0.23 ± 0.02	0.58 ± 0.03	0.83 ± 0.03	0.44 ± 0.02	0.36 ± 0.02	0.04 ± 0.01	153.2 (−119.9)
Austenite from L-Step	80.05 ± 0.15	15.87 ± 0.13	1.64 ± 0.05	0.23 ± 0.02	0.46 ± 0.02	0.85 ± 0.03	0.46 ± 0.02	0.25 ± 0.02	0.04 ± 0.01	351.4 (78.3)
Tempered Martensite, α-Fe	90.89 ± 0.32	6.82 ± 0.28	0.36 ± 0.07	0.15 ± 0.04	0.62 ± 0.09	0.56 ± 0.08	0.34 ± 0.06	0.03 ± 0.02	0.08 ± 0.03	
ThermoCalc 863 K (590 °C)										
Austenite	78.49	18.09	1.39	0.1	0.68	0.71	0.2	0.29	0.002	
α-Fe	95.18	3.72	0.074	0.001	0.25	0.53	0.13	0.024	0.006	

Compositions of austenite and α-Fe, obtained from equilibrium thermodynamic calculations at 863 K (590 °C) using ThermoCalc are also listed.

V. DISCUSSION

A. 3-D Atom Probe Tomography (APT)

1. APT analyses of the QL-treated samples

Nickel concentration in austenite in QL-1 sample, as obtained from the proximity histogram shown in Figure 5(a), is 12.5 at. pct, which is in reasonable agreement with 11.8 at. pct Ni, predicted by thermodynamic equilibrium calculations at 923 K (650 °C), Table IV. The austenite in the QL-2 sample has, however, a significantly higher Ni concentration, which increases gradually from 15.3 at. pct near the α-Fe/austenite heterophase interface to 17.9 at. pct toward the inner core of austenite, Figure 5(b). We note that the right-hand side of the proximity histogram in Figure 5(b) represents the concentration of the inner core of the austenite region, Figure 4(b). A similar trend as for Ni is also observed for the Mn concentration profile, Figure 5(b). Due to the limited holding time of 30 minutes at 923 K (650 °C), composition of austenite can deviate from the equilibrium calculated values. Higher average Ni concentration in austenite, as observed in the QL-2 sample, could be facilitated by short-circuit diffusion of Ni along lath-boundaries and dislocations. In comparison to QL-2 sample, there is little variation in the Ni concentration within the austenite in QL-1 sample, Figure 5(a). It is slightly lesser near the center of the austenitic region, ~12 at. pct than at the α-Fe/austenite heterophase interface and toward the extreme right-hand side of the proximity histogram, ~13 at. pct. Fultz et al.[35] observed a higher Ni concentration toward the surfaces of austenite particles as compared to their inner regions in their STEM-EDS study of a 9 wt pct Ni steel, intercritically tempered at 863 K (590 °C). They suggested that with increasing aging time, the available carbon concentration in martensite decreases and therefore, continued growth of austenitic particles required a higher Ni concentration. They, however, could not measure the carbon concentration in austenite due to limitation of the EDS technique. In the present study, we do not observe this trend in the QL-2 sample, as the Ni concentration near the center of the austenitic region is greater than at the α-Fe/austenite heterophase interface. Additionally, unlike the 9 wt pct Ni steels analyzed by Fultz et al.,[35] the steel investigated in the present study also contains significant additions of strong carbide forming elements, specifically Mo, Cr, and V. The presence of the metal carbides in the microstructure increases the complexity of analyzing small variations in the C and Ni concentrations in austenite. Linear concentration profiles of Ni, C, Mo, Cr, and V across a M_2C-type carbide observed in austenite in the QL-2 sample are displayed in Figure 8, which reveal strong partitioning of C and Ni toward and away from the carbide phase, respectively. Thus, even though the metal carbides were excluded before obtaining the proximity histograms displayed in Figure 5, concentrations of C and Ni in austenite in proximity to the carbides can be affected.
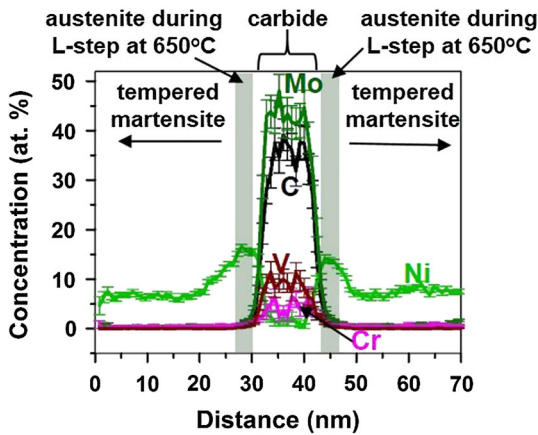
Fig. 8—Linear concentration profiles of Mo, C, V, Cr, and Ni across the tempered martensite (α-Fe), Ni-rich region (austenite), and an M_2C-type carbide precipitate in the QL-2 10 wt pct Ni steel sample exhibiting strong partitioning of C and Ni toward and away from the carbide phase, respectively.

Table VI. Comparison of M_s Temperature Predictions for Austenite Obtained After the T-Step at 863 K (590 °C) in the QLT-Treated 10 Wt Pct Ni Steel Samples Using the Ghosh–Olson Approach and Empirical Relations

	M_s [K (°C)] QLT-1	M_s [K (°C)] QLT-2
Present (Ghosh–Olson Approach)[49–51]	126 (−147)	153 (−120)
Payson et al.[68]	267 (−6)	278 (5)
Grange et al.[69]	210 (−63)	224 (−49)
Nehrenberg[70]	273 (0)	283 (10)
Steven et al.[71]	328 (55)	337 (64)
Andrews[72]	306 (33)	313 (40)

2. APT analyses of the QLT-treated samples

Shaded regions in the proximity histogram, Figure 7, represent the nanolayers of austenite that form during the T-step tempering treatment at 863 K (590 °C). The new austenite formed has a higher Ni concentration (~22 at. pct) than the austenite formed during the L-step (~12 to 17 at. pct). This result is in general agreement with the thermodynamic equilibrium calculations, which predict a higher Ni concentration in austenite at 863 K (590 °C) than at 923 K (650 °C), Tables IV and V. We emphasize that the Ni diffusivity, D in austenite at 863 K (590 °C) is extremely small, therefore, its estimated root-mean-squared diffusion distance, $\sqrt{2Dt}$ in austenite for 1 hour is only ~1 nm.[64,65] As a result, the Ni concentration in austenite does not homogenize and we are able to differentiate the austenitic Ni compositions formed during the L- and T-steps in the proximity histograms, Figure 7. Therefore, the Ni-rich regions lying in the vicinity of the shaded regions in the proximity histograms represent austenite that is retained from the L-step and contains ~14.5 to 17.0 at. pct Ni. Diffusivity of Ni in ferrite at 863 K (590 °C) is more than three orders of magnitude greater than in austenite and its estimated root-mean-squared diffusion distance, $\sqrt{2Dt}$ in ferrite for 1 hour is 37 nm.[64] Thus, during

the T-step tempering, Ni diffuses from the martensitic matrix toward retained austenite (as dictated by thermodynamics), but due to its negligible diffusion in austenite, gets accumulated at its surface. This leads to the growth of austenite (with a higher Ni concentration) on top of the retained austenite from the L-step.

A previous APT investigation of a similar 10 wt pct Ni steel also indicated a similar growth mode of a thin layer of austenite with a higher Ni concentration at a tempering temperature of 811 K (538 °C) over the austenite inherited from prior annealing at 894 K (621 °C).[43] Austenite reversion via growth at martensite–austenite interface has also been reported in Fe-12 wt pct Mn steel.[60,66] Using APT, the authors showed that retained austenite (from as-quenched condition) acted as a template for the growth of austenite during aging at 723 K (450 °C).

B. Martensite-Start (M_s) Temperature Calculations

Using the Ghosh–Olson thermodynamic and kinetic approach,[49–51] and the composition of austenite measured utilizing APT, the predicted M_s temperatures for austenite in the QL-1 and QL-2 samples are 459. K and 345 K (186.5 °C and 71.9 °C), respectively, Table IV. The calculated M_s temperature for the QL-1 sample is in excellent agreement with the dilatometric results, which indicated that the M_s temperature for the austenite formed during the L-step is 461 K (188 °C), Figure 2. Austenite in the QL-2 sample is richer in Ni and thus has a lower M_s temperature. Nevertheless, it is certain that the austenite formed after the L-step is too lean in its solute content to be stable at sub-ambient temperatures. We emphasize that the martensitic transformation commences at M_s and continues to occur on further cooling and is complete at the martensite-finish (M_f) temperature.[67] Thus, depending on the final temperature reached on cooling, some of the austenite can be retained below the M_s temperature, as is the case for the QL-treated sample in which 8.1 vol pct austenite is retained at room temperature, Table III. It has been observed in 9 wt pct Ni steels that individual austenite particles may undergo only a partial martensitic transformation.[28,35] Regions within the austenite particles with leaner Ni concentrations were found to be less stable and transformed to martensite, while other regions remained untransformed.[35]

For the austenite formed during the T-step in the fully QLT-treated samples (shaded regions in the proximity histograms in Figure 7, compositions in Table V), M_s temperature is calculated to be 126 K and 153 K (−147 °C and −120 °C) for the austenite in QLT-1 and QLT-2 samples, respectively. These predictions are in agreement with the X-ray diffraction results, which revealed that the austenite after the T-step remains thermally stable even at 188.7 K (−84.4 °C). In contrast, commonly used linear empirical relations in the archival literature[45,68–72] are unable to predict accurately, the M_s temperatures for the austenite formed during the T-step, Table VI. In general, the applicability of these empirical relations is restricted to leaner solute compositions of austenite[72] and thus, they are not
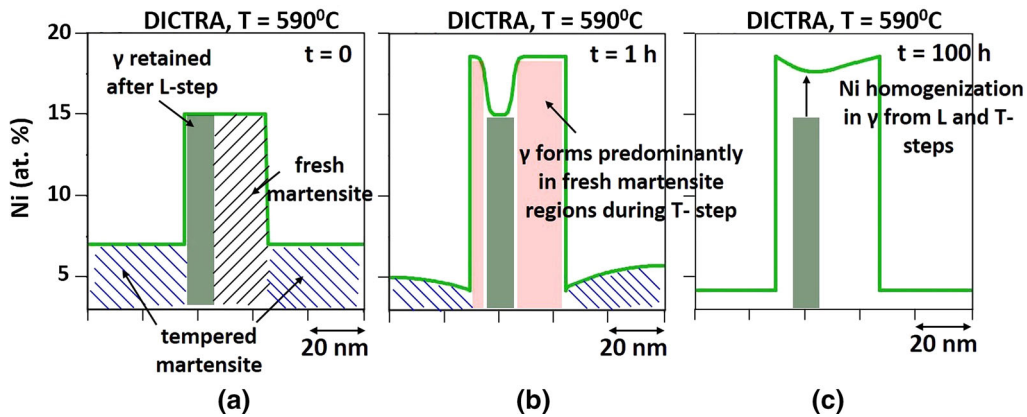
Fig. 9—DICTRA simulations during T-step tempering at 863 K (590 °C) displaying a Ni concentration profile after: (a) 0 s; (b) 1 h; and (c) 100 h. A DICTRA simulation after 1 h in (b) indicates that austenite grows predominantly into the fresh martensitic region.

meaningful for the highly Ni-rich austenite obtained in the present study after the T-step.

C. DICTRA Simulations

To simulate austenite formation during the T-step, the DICTRA cell at t = 0 s is constructed to represent the microstructure of the QL-treated sample, Figure 9(a). It consists of tempered martensite, fresh-martensite, and retained austenite with Ni concentrations of 7, 15, and 15 at. pct, respectively, as approximated from the APT analyses of the QL-treated samples, Table IV. The dimension of the retained austenitic region in the DICTRA cell, Figure 9(a), is fixed at 10 nm, similar to regions representing retained austenite from the L-step in the proximity histograms, Figure 7. The extent of the fresh martensitic region is kept to 20 nm and the total length of tempered martensitic region, 70 nm is obtained after fixing the overall Ni concentration at 9.4 at. pct in the alloy. Following the discussion in Section V–A–2, we use the retained austenite from the L-step as a template for austenite growth during the T-step.

DICTRA simulations after 1 hour at 863 K (590 °C) indicate that austenite grows predominantly into the Ni-rich fresh martensitic region, Figure 9(b), and contains 18 at. pct Ni. In Figure 9(b), we also observe that the Ni concentration of the newly formed austenite (18 at. pct) during the 1 hour simulation at 863 K (590 °C) does not homogenize with the Ni concentration of the austenite inherited from the L-step (15 at. pct). We also similarly interpret the APT proximity histograms of the QLT-treated samples, Figure 7. DICTRA simulation after 100 hours exhibit, however, a more homogeneous Ni concentration in the austenitic phase, Figure 9(c).

D. Austenite Formation During the T-Step

Austenite formation is significantly more profuse during isothermal treatment at higher intercritical temperatures, due to the higher predicted equilibrium volume fraction of austenite coupled with the faster diffusion kinetics of Ni. Thus, even though some of the austenite formed is not thermally stable after the L-step, densely distributed Ni-rich regions are created, Figure 1(a), in the form of fresh-martensite or retained austenite. The presence of Ni-rich martensitic regions in proximity of retained austenite reduces the root-mean-squared diffusion distance for Ni toward retained austenite, which enhances the growth kinetics of austenite during the T-step. Thus, significant austenite growth occurs within 1 hour as the austenite volume fraction increases from 8.1 pct in the QL-treated sample to 18.5 pct in the QLT-treated sample. In contrast, we obtain only 2.9 vol pct austenite in the QT-treated sample, tempered at 863 K (590 °C) for 1 hour without a prior intercritical step at a higher temperature. Thus, a multistep intercritical treatment facilitates the formation of a significant volume fraction of thermally stable austenite in relatively short holding times, which are of great practical relevance. Similar multistep intercritical treatments have also been employed for 5.5 wt pct Ni ferritic steels[29,34,36] and ultrahigh strength AF1410 martensitic steels[13] to form finely dispersed austenite, enriched with stabilizing solutes.

It can now be inferred that the growth of the austenitic layer during the T-step, Figure 7(a), occurred at the expense of the fresh martensitic region, which was sandwiched between the retained austenite regions, inherited from the L-step. Alternatively, if the retained austenite region is placed between the fresh martensitic regions [as in the DICTRA cell, Figure 10(a)], the austenitic layers grow on both sides of the retained austenite during the T-step, Figure 10(b). The DICTRA-simulated Ni concentration profile, Figure 10(b), is qualitatively similar to the Ni concentration profile obtained in the proximity histogram of the QLT-2 sample, Figure 7(b), and is reproduced herein, Figure 10(c), for comparative purposes. The Ni concentration of the newly formed austenite layer is, however, higher in the APT profile (~22 at. pct) than that obtained by DICTRA simulations, 18 at. pct. These differences can arise as the DICTRA simulations are performed on a simpler Fe-Ni system, assume an
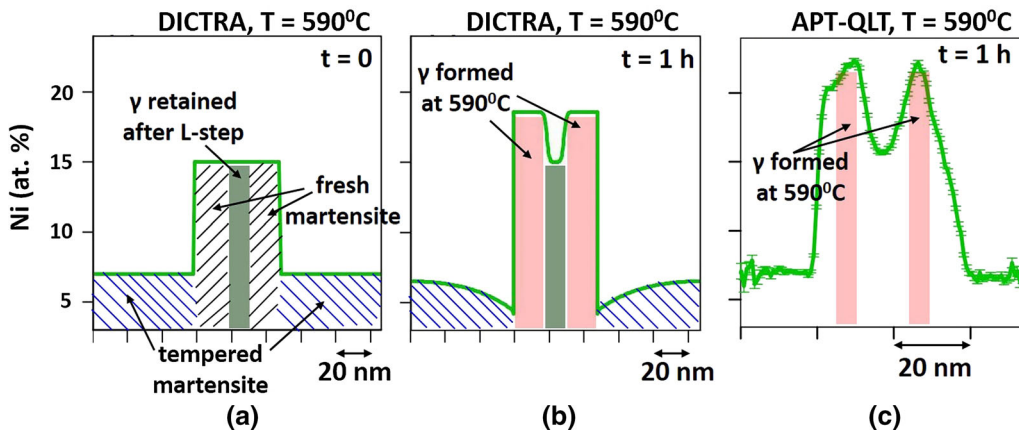
Fig. 10—DICTRA simulations during T-step tempering at 863 K (590 °C) displaying a Ni concentration profile after: (*a*) 0 s; (*b*) 1 h; and (*c*) Ni concentration profile obtained from an APT investigation of the QLT-treated 10 wt pct Ni steel [QLT-2 sample, Fig. 7(b)]. Nickel concentration profiles obtained from both APT and DICTRA simulations indicate the formation of nanolayers of austenite with a higher Ni concentration on top of the retained austenite from the L-step containing lower Ni concentration.

infinite mobility of the heterophase interface, and neglect effects from curved interfaces.[39,60]

VI. SUMMARY AND CONCLUSIONS

In this article, we elucidated the basic physical principles that control the thermal stability of austenite and kinetics of its formation during the QLT-type multistep intercritical treatment for a low-carbon 10 wt pct Ni steel. The role of Ni-rich austenite, and fresh martensitic regions, inherited from the L-step at 923 K (650 °C), in forming thermally stable austenite during the T-step tempering at 863 K (590 °C) is highlighted. The major findings are as follows:

1. Austenite formed during the first intercritical treatment (L-step) at 923 K (650 °C) starts transforming to martensite at 461 K (188 °C), Figure 2. A significant volume fraction of austenite (8.1 pct) is, however, retained and still present after quenching the sample to room temperature, as determined by synchrotron X-ray diffraction experiments performed at the Advanced Photon Source at Argonne National Laboratory.
2. The volume fraction of austenite in the QLT-treated sample at room temperature is 18.5 pct; 18 vol pct austenite is also obtained in the QLT-treated sample that was quenched to 188.7 K (−84.4 °C), prior to the X-ray diffraction experiment at the Advanced Photon Source, Table III. This indicates that austenite after the T-step is thermally stable, and its M_s is below 188.7 K (−84.4 °C).
3. The composition of austenite formed during the L-step intercritical treatment at 923 K (650 °C), as obtained by atom probe tomography is 84.1Fe-12.5Ni-1.0Mn-0.36C-0.35Si-0.77Cr-0.43Mo-0.23Cu-0.04V (at. pct) for the QL-1 sample, and 79.2Fe-16.7Ni-1.2Mn-0.39C-0.34Si-0.79Cr-0.67Mo-0.26Cu-0.06V (at. pct) for the QL-2 sample, Table IV. The

corresponding M_s temperatures, as calculated using the Ghosh–Olson thermodynamic and kinetic approach are 459.6 K and 345 K (186.5 °C and 71.9 °C) for austenite in the QL-1 and QL-2 samples, respectively.
4. Atom probe tomographic concentration profiles obtained for the QLT-treated samples indicate that nanolayers of austenite, with a higher Ni concentration grow during the T-step at 863 K (590 °C), on top of the retained austenite from the L-step, Figure 7. The composition of austenite formed during the T-step, as obtained by atom probe tomography is 73.4Fe-21.7Ni-2.4Mn-0.2C-0.45Si-0.99Cr-0.43Mo-0.33Cu-0.04V (at. pct) for QLT-1 sample and 73.4Fe-21.9Ni-2.0Mn-0.23C-0.58Si-0.83Cr-0.44Mo-0.36Cu-0.04V (at. pct) for the QLT-2 sample, Table V.
5. The M_s temperature for the austenite formed during the T-step in the QLT-treated samples, as calculated using the Ghosh–Olson thermodynamic and kinetic approach is less than 173 K (−100 °C), which is in an excellent agreement with our experimental results. Alternatively, linear empirical relations in the archival literature are not meaningful for estimating M_s temperatures for the austenite with such high Ni concentrations, Table VI.
6. DICTRA simulations in conjunction with atom probe tomography experiments reveal that austenite growth during the T-step tempering at 863 K (590 °C) occurs predominantly in the Ni-rich fresh martensitic regions, Figure 9. The presence of Ni-rich fresh martensitic regions in vicinity of retained austenite enhances growth kinetics of thermally stable austenite formed during the T-step, and results in the significant increase of austenite volume fraction from 8.1 to 18.5 pct in a relatively short holding time of 1 hour at 863 K (590 °C). In contrast, only 2.9 vol pct austenite is obtained in the sample tempered at 863 K (590 °C), without a prior L-step treatment.

ACKNOWLEDGMENTS

REFERENCES

1. E.J. Czyryca, R.E. Link, R.J. Wong, D.A. Aylor, T.W. Montemarano, and J.P. Gudas: *Nav. Eng. J.*, 1990, vol. 102, pp. 63–82.
2. P.J. Konkol, K.M. Stefanick, and G.S. Pike: *Weld. J.*, 2011, vol. 90, pp. 34–41.
3. M.D. Mulholland: Ph.D. Thesis, Northwestern University, Evanston, IL, 2011.
4. T.W. Montemarano, B.P. Sack, and J.P. Gudas: *J. Ship Prod.*, 1986, vol. 2, pp. 145–62.
5. P. Sadhukhan: Ph.D. Thesis, Northwestern University, Evanston, IL, 2008.
6. A.H. Hunter: Ph.D. Thesis, Northwestern University, Evanston, IL, 2012.
7. N.J. Wengrenovich and G.B. Olson: *Mater. Today Proc*, 2015, vol. 2, pp. S639–42.
8. X.J. Zhang: *Mater. Sci. Technol.*, 2013, vol. 28, pp. 818–22.
9. D. Jain, D. Isheim, A.H. Hunter, and D.N. Seidman: *Metall. Mater. Trans. A*, 2016, vol. 47A, pp. 3860–72.
10. Z.D. Feinberg: Ph.D. Thesis, Northwestern University, Evanston, IL, 2012.
11. J.T. Bono, J.N. DuPont, D. Jain, S.I. Baik, and D.N. Seidman: *Metall. Mater. Trans. A*, 2015, vol. 46A, pp. 5158–70.
12. M. Grujicic: *Mater. Sci. Eng. A*, 1990, vol. 128, pp. 201–07.
13. G.N. Haidemenopoulos, G.B. Olson and M. Cohen: in *Innovations in Ultra-high Strength Steel Technology,* Proc. 34th Sagamore Army Materials Research Conf., G.B. Olson, M. Azrin, and E.S. Wright, eds., US Army Materials Technology Laboratory, Watertown, MA, 1987, pp. 549–93.
14. A. Saha and G.B. Olson: *J. Comput. Aided Mater. Des.*, 2007, vol. 14, pp. 177–200.
15. B.C. De Cooman: *Curr. Opin. Solid State Mater. Sci.*, 2004, vol. 8, pp. 285–303.
16. R. Kuziak, R. Kawalla, and S. Waengler: *Arch. Civ. Mech. Eng.*, 2008, vol. 8, pp. 103–17.
17. O. Matsumura, Y. Sakuma, and H. Takechi: *Trans. Iron Steel Inst. Jpn*, 1987, vol. 27, pp. 570–79.
18. G.B. Olson and M. Azrin: *Metall. Trans. A*, 1978, vol. 9, pp. 713–21.
19. V.F. Zackay, E.R. Parker, D. Fahr, and R. Busch: *ASM Trans. Quart.*, 1967, vol. 60, pp. 252–59.
20. J.R. Patel and M. Cohen: *Acta Metall.*, 1953, vol. 1, pp. 531–38.
21. B.A. Graville: in *Proc. Int. Conf. on Welding of HSLA (Microalloyed) Structural Steels,* ASM International, Metals Park, OH, 1978, pp. 85–101.
22. T.L. Anderson, J.A. Hyatt, and J.C. West: *Weld. J.*, 1987, vol. 66, pp. 21–26.
23. D.V. Edmonds, K. He, F.C. Rizzo, B.C. De Cooman, D.K. Matlock, and J.G. Speer: *Mater. Sci. Eng. A*, 2006, vol. 438, pp. 25–34.
24. J. Speer, D.K. Matlock, B.C. De Cooman, and J.G. Schroth: *Acta Mater.*, 2003, vol. 51, pp. 2611–22.
25. W. Jolley: *J. Iron Steel Inst.*, 1968, vol. 206, pp. 170–73.
26. W.C. Leslie, R.J. Sober, S.G. Babcock, and S.J. Green: *ASM Trans. Quart.*, 1969, vol. 62, pp. 690–10.
27. R.W. Fonda and G. Spanos: *Metall. Mater. Trans. A*, 2014, vol. 45A, pp. 5982–89.
28. B. Fultz, J.I. Kim, Y.H. Kim, H.J. Kim, G.O. Fior, and J.W. Morris: *Metall. Trans. A*, 1985, vol. 16A, pp. 2237–49.
29. J.I. Kim, C.K. Syn, and J.W. Morris: *Metall. Trans. A*, 1983, vol. 14, pp. 93–103.
30. C.K. Syn, B. Fultz, and J.W. Morris: *Metall. Trans. A*, 1978, vol. 9, pp. 1635–40.
31. C.K. Syn, J.W. Morris, and S. Jin: *Metall. Trans. A*, 1976, vol. 7, pp. 1827–32.
32. J.R. Strife and D.E. Passoja: *Metall. Trans. A*, 1980, vol. 11, pp. 1341–50.
33. K.J. Kim and L.H. Schwartz: *Mater. Sci. Eng.*, 1978, vol. 33, pp. 5–20.
34. J.I. Kim, H.J. Kim, and J.W. Morris: *Metall. Trans. A*, 1984, vol. 15, pp. 2213–19.
35. B. Fultz, J.I. Kim, Y.H. Kim, and J.W. Morris: *Metall. Trans. A*, 1986, vol. 17, pp. 967–72.
36. J.I. Kim and J.W. Morris: *Metall. Trans. A*, 1981, vol. 12, pp. 1957–63.
37. B. Sundman, B. Jansson, and J.O. Andersson: *Calphad*, 1985, vol. 9, pp. 153–90.
38. J.O. Andersson, T. Helander, L. Höglund, P. Shi, and B. Sundman: *Calphad*, 2002, vol. 26, pp. 273–312.
39. A. Borgenstam, A. Engstrom, L. Hoglund, and J. Agren: *J. Ph. Equilib.*, 2000, vol. 21, pp. 269–80.
40. B. Gault, M.P. Moody, J.M. Cairney, and S.P. Ringer: *Atom Probe Microscopy*, Springer, NewYork, NY, 2012.
41. D.N. Seidman: *Annu. Rev. Mater. Res.*, 2007, vol. 37, pp. 127–58.
42. T.F. Kelly and M.K. Miller: *Rev. Sci. Instrum.*, 2007, vol. 78, p. 031101.
43. D. Isheim, A.H. Hunter, X.J. Zhang, and D.N. Seidman: *Metall. Mater. Trans. A*, 2013, vol. 44A, pp. 3046–59.
44. S. Lee, S. Shin, M. Kwon, K. Lee, and B.C. De Cooman: *Metall. Mater. Trans. A*, 2017, vol. 48A, pp. 1678–1700.
45. C. Capdevila, F.G. Caballero, and C.G.D. Andrés: *ISIJ Int.*, 2002, vol. 42, pp. 894–902.
46. M. Palumbo: *Calphad*, 2008, vol. 32, pp. 693–708.
47. K. Ishida: *J. Alloys Comp.*, 1995, vol. 220, pp. 126–31.
48. T. Sourmail and C. Garcia-Mateo: *Comput. Mater. Sci.*, 2005, vol. 34, pp. 323–34.
49. G. Ghosh and G.B. Olson: *Acta Metall. Mater.*, 1994, vol. 42, pp. 3361–70.
50. G. Ghosh and G.B. Olson: *Acta Metall. Mater.*, 1994, vol. 42, pp. 3371–79.
51. G. Ghosh and G.B. Olson: *J. Ph. Equilib.*, 2001, vol. 22, pp. 199–207.
52. G.B. Olson and M. Cohen: *Metall. Trans. A*, 1976, vol. 7, pp. 1905–14.
53. B.D. Cullity and S.R. Stock: *Elements of X-ray Diffraction*, 3rd ed., Prentice Hall, New Jersey, 2001, p. 351.
54. H.P. Klug and L.E. Alexander: *X-ray diffraction procedures*, 2nd ed., John Wiley and Sons, New York, NY, 1974, p. 540.
55. M.K. Miller, K.F. Russell, and G.B. Thompson: *Ultramicroscopy*, 2005, vol. 102, pp. 287–98.
56. R.L. Fleischer: *Acta Metall.*, 1963, vol. 11, pp. 203–09.

57. R.L. Fleischer: *The Strengthening of Metals*, Reinhold Publishing Corp, New York, NY, 1964, p. 93.
58. G. Ghosh: *Northwestern University*, IL, Evanston, 2000 Unpublished Research.
59. J. Ågren: *Acta Metall.*, 1982, vol. 30, pp. 841–51.
60. O. Dmitrieva, D. Ponge, G. Inden, J. Millán, P. Choi, J. Sietsma, and D. Raabe: *Acta Mater.*, 2011, vol. 59, pp. 364–74.
61. O.C. Hellman, J.A. Vandenbroucke, J. Rüsing, D. Isheim, and D.N. Seidman: *Microsc. Microanal.*, 2000, vol. 6, pp. 437–44.
62. H.K.D.H. Bhadeshia and R.W.K. Honeycombe: *Steels: Microstructure and Properties*, Elsevier, Amsterdam, 2006, p. 74.
63. R.P. Kolli and D.N. Seidman: *Acta Mater.*, 2008, vol. 56, pp. 2073–88.
64. K. Hirano, M. Cohen, and B.L. Averbach: *Acta Metall.*, 1961, vol. 9, pp. 440–45.
65. S.J. Rothman, L.J. Nowicki, and G.E. Murch: *J. Phys. F*, 1980, vol. 10, pp. 383–98.
66. D. Raabe, S. Sandlöbes, J. Millán, D. Ponge, H. Assadi, M. Herbig, and P.P. Choi: *Acta Mater.*, 2013, vol. 61, pp. 6132–52.
67. G. Krauss: *Steels: Processing, Structure, and Performance*, Materials Park, OH, ASM International, 2005, p. 63.
68. P. Payson and C.H. Savage: *Trans. ASM*, 1944, vol. 33, pp. 261–80.
69. R.A. Grange and H.M. Stewart: *Trans. AIME*, 1946, vol. 167, pp. 467–501.
70. A.E. Nehrenberg: *Trans. AIME*, 1946, vol. 167, p. 494.
71. W. Steven and A.G. Haynes: *J. Iron Steel Inst.*, 1956, vol. 183, pp. 349–59.
72. K.W. Andrews: *J. Iron Steel Inst.*, 1965, vol. 203, pp. 721–27.